Nitrogen-doping driven topological transition, Lifshitz transition, and superconducting dome in orthorhombic α-Mo_2C

Ya-Ping Li,[1] Kai-Yue Jiang,[1] Shu-Xiang Qiao,[1] Yu-Lin Han,[1] Hong-Yan Lu,[1,*] and Ping Zhang[1,2,†]
[1]*School of Physics and Physical Engineering, Qufu Normal University, Qufu 273165, China*
[2]*Institute of Applied Physics and Computational Mathematics, Beijing 100088, China*

(Received 29 September 2025; revised 26 January 2026; accepted 23 February 2026; published 1 April 2026)

Experimental studies have reported that nitrogen (N)-doped orthorhombic α-Mo_2C exhibits a significant enhancement in its superconducting transition temperature (T_c). To elucidate the underlying mechanisms, we conducted a systematic first-principles investigation of N-doped α-Mo_2C, focusing on its structural stability, electronic structure, phonon dynamics, and superconductivity. The results show that the superconductivity originates from the electron-phonon coupling (EPC) between Mo-4*d* orbital electrons and low-frequency vibrational modes of Mo atoms. As the N content increases, the T_c exhibits a dome-shaped variation, well-consistent with experimental observations. Notably, varying the N-doping concentration drives a Lifshitz transition and a trivial-nontrivial-trivial topological evolution, as confirmed by Wannier-based Z_2 invariants. These findings provide important insights into the superconductivity and topology in N-doped α-Mo_2C, and offer valuable guidance for the design of high-performance superconducting and topological quantum materials.

DOI: 10.1103/fssg-1b79

I. INTRODUCTION

Transition metal carbides (TMCs) have garnered considerable attention in recent years due to their unique combination of metallic and ceramic properties. These materials exhibit high melting points, exceptional hardness, excellent electrical conductivity, superior corrosion resistance and remarkable chemical stability, enabling their use in extreme environments such as high-temperature structural applications, electrocatalysis, energy storage systems [1–5]. Furthermore, their tunable electronic structures, arising from the partially filled *d*-orbitals of transition metals, make them promising candidates for advanced functional materials, including superconductors. Among the TMCs family, molybdenum carbide (Mo_2C) has emerged as a particularly compelling material due to its structural robustness and versatile physical properties. Mo_2C demonstrates noble-metal-like catalytic activity in reactions such as hydrogenation [6,7], hydrogen evolution reactions [8–11], and water-gas shift [12,13], while also exhibiting intriguing low-temperature superconductivity [2,14]. Specifically, the orthorhombic phase of Mo_2C (α-Mo_2C) features rigid [Mo_6C] octahedral motifs that facilitate electron-phonon coupling (EPC) [15]. The EPC mechanism is essential for conventional superconductivity within the Bardeen-Cooper-Schrieffer (BCS) framework [16]. With a Vickers hardness of 13.4 GPa, α-Mo_2C represents a rare example of a hard superconductor and provides a promising platform for studying structure-property relationships in quantum materials [15]. These exceptional properties provide a strong foundation for further tuning its superconducting performance through electronic structure engineering, including doping and strain modulation.

Among various strategies to modulate the superconducting properties of Mo_2C, N-doping has emerged as a particularly promising approach. While previous researches primarily focused on N-doping to enhance the catalytic and electronic transport performance of Mo_2C for applications such as hydrogen evolution reactions, lithium-ion storage, and stable alkali metal anodes [17–20]. Recent studies have demonstrated that N incorporation can also effectively enhance its superconducting performance [21,22]. Earlier experimental work often relied on complex precursors and multi-step processes, yielding C-rich or multiphase composites with limited N incorporation and poor crystallinity, thus precluding accurate evaluation of intrinsic superconducting properties [21]. Recently, solid-state reactions and simple urea approaches [21,22] have enabled the synthesis of phase-pure $Mo_2C_{1-x}N_x$ solid solutions with tunable N content up to $x = 0.57$ [21]. These doped samples retain the orthorhombic α-Mo_2C structure while exhibiting significantly enhanced superconducting properties. The superconducting transition temperature (T_c) increases substantially from 5.5 K in undoped α-Mo_2C to 7.9 K at optimal doping levels, accompanied by elevated upper critical fields and clear evidence of bulk superconductivity [21]. Beyond these experimental findings, Mo_2C has recently attracted significant attention as a promising platform for topological superconductivity owing to its tunable band structure, strong metallic bonding, and symmetry-allowed surface states [23]. However, both theoretical predictions and experimental results remain inconclusive regarding whether the topological electronic bands of α-Mo_2C persist after N-doping. Therefore, to elucidate the underlying mechanisms of doping enhanced superconductivity and explore the possibility of topologically nontrivial phases, first-principles calculations are essential for systematically investigating the electronic structure, phonon behavior, and EPC in N-doped α-Mo_2C system.

*Contact author: hylu@qfnu.edu.cn
†Contact author: zhang_ping@iapcm.ac.cn

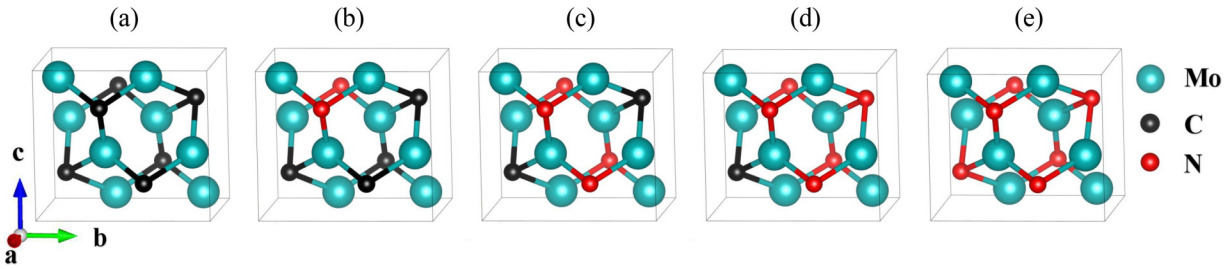

FIG. 1. (a)–(e) The crystals of $Mo_2C_{1-x}N_x$ ($x = 0, 0.25, 0.5, 0.75, 1$). The primitive cell is shown by the black solid line.

Here, we conduct a comprehensive study based on first-principles calculations. Our results reveal that with increasing N concentration: (1) The crystal structure of α-Mo_2C remains stable without undergoing any structural phase transition; (2) A topological transition occurs, accompanied by a Lifshitz transition in the Fermi surface; (3) The T_c exhibits a dome-shaped dependence on N content, consistent well with experimental observations. This trend is primarily governed by the variation in the electronic density of states (DOS) at the Fermi level and low-frequency vibrational modes of Mo atoms. These findings not only deepen the understanding of N-doping on the superconductivity in $Mo_2C_{1-x}N_x$, but also provide new insights into the electronic topological properties that may exist in TMCs.

II. COMPUTATIONAL DETAILS

The electronic and superconducting properties of $Mo_2C_{1-x}N_x$ ($x = 0, 0.25, 0.5, 0.75, 1$) are investigated using first-principles calculations, as implemented in the Vienna Ab-initio Simulation Package (VASP) [24] and the Quantum ESPRESSO (QE) software package [25]. The electron-ion interactions are treated using the Projector-Augmented Wave (PAW) method [26], and the exchange-correlation effects are described within the generalized gradient approximation (GGA) using the Perdew-Burke-Ernzerhof (PBE) parametrization [27]. The topology properties are calculated through the WANNIERTOOLS package [28,29], and its basis set depends on the maximum localized Wannier functions (MLWFs) [30,31] from the VASP2WANNIER90 interfaces [32]. More computational methods and details are shown in the Supplemental Material (SM) [33] (which also contains Refs. [34–36]).

III. RESULTS AND DISCUSSIONS

A. Crystal structures

Based on first-principles calculations, we investigate whether N-doping induces a structural phase transition in α-Mo_2C. The results show that the orthorhombic structure of α-Mo_2C remains stable across all examined doping concentrations, with no indication of a phase transition, consistent with experimental observations [21,22]. Therefore, the studied compounds $Mo_2C_{1-x}N_x$ ($x = 0, 0.25, 0.5, 0.75, 1$) all retain an orthorhombic ξ-Fe_2N-type crystal structure with the space group *Pbcn* (No. 60), as illustrated in Fig. 1. At doping levels of $x = 0.25$, 0.75, and 1, the substituted structures remain symmetry-equivalent no matter which carbon atom is replaced. However, at $x = 0.5$, three inequivalent configurations occur due to the presence of multiple nonequivalent carbon sites. We evaluate the thermodynamic stability of these three inequivalent configurations by calculating their formation energies according to the formula: $E_{\text{form}} = [E_{Mo_2C_{0.5}N_{0.5}} - (8E_{Mo} + 2E_C + 2E_N)]/12$, where the $E_{Mo_2C_{0.5}N_{0.5}}$, E_{Mo}, E_C, and E_N denote the total energies of $Mo_2C_{0.5}N_{0.5}$, bulk Mo metal, orthorhombic graphite and an isolated N_2 molecule, respectively. The calculated formation energies for the three inequivalent configurations are −0.1746, −0.1741, and −0.1711 eV/atom, respectively. Among them, the configuration shown in Fig. 1(c) exhibits the lowest formation energy, indicating the highest thermodynamic stability and suggesting that it is the most favorable for experimental realization. Consequently, only this representative configuration is discussed in the main text, while the results of the other two configurations are presented in Figs. S1–S3 of the SM [33].

From the crystal structures of $Mo_2C_{1-x}N_x$ in Figs. 1(a)–1(e), it is clearly seen that each primitive unit cell contains eight Mo atoms and four C/N atoms, where N atoms substitute for C at varying concentrations. Each C/N atom is coordinated by six Mo atoms, and each Mo atom is bonded to three C/N atoms. The calculated lattice parameters and unit cell volumes (V) are summarized in Table I. As shown, the calculated results for pristine α-Mo_2C are in good agreement with experimental data [14,21,22,37]. Upon increasing N content, the lattice parameter a shows a gradual increase, while b and the unit cell volume V exhibit a monotonic decrease. These trends are consistent with those observed in experimental measurements [21,22], confirming the reliability of the calculation results.

B. Electronic structures and topological transition

To investigate the origin of superconductivity in pristine α-Mo_2C and assess the influence of N-doping, we calculate the electronic properties of $Mo_2C_{1-x}N_x$ for N-doping

TABLE I. Lattice parameters a, b, and c (Å) and the unit cell volume V (Å^3) for $Mo_2C_{1-x}N_x$ ($x = 0, 0.25, 0.5, 0.75, 1$).

Materials	a (Å)	b (Å)	c (Å)	V (Å^3)
α-Mo_2C	4.74	6.06	5.23	150.23
$Mo_2C_{0.75}N_{0.25}$	4.76	6.05	5.20	149.75
$Mo_2C_{0.5}N_{0.5}$	4.78	6.03	5.16	148.73
$Mo_2C_{0.25}N_{0.75}$	4.82	6.01	5.12	148.32
Mo_2N	4.89	5.97	5.06	147.72

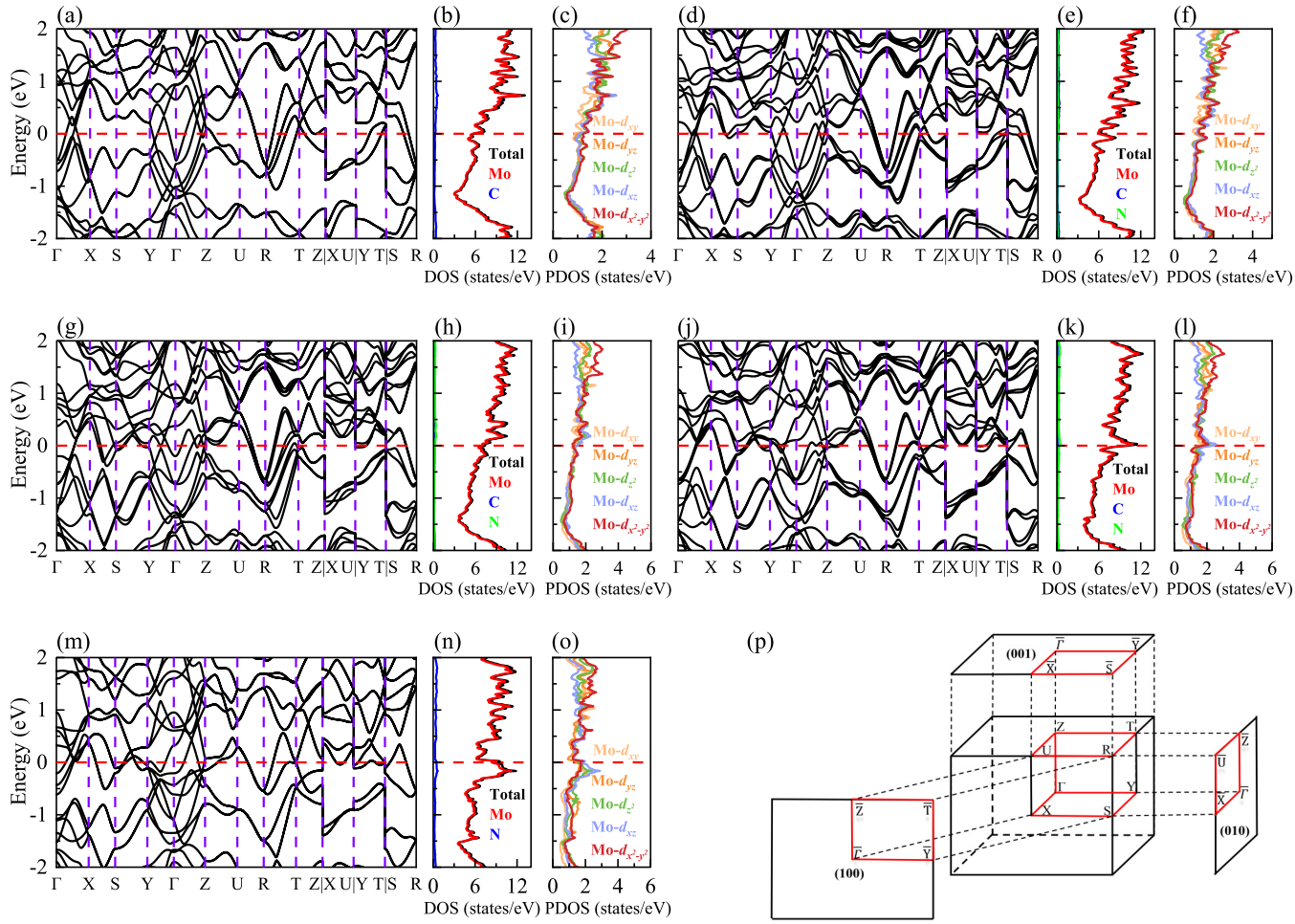

FIG. 2. (a), (d), (g), (j), (m) Band structures without SOC; (b), (e), (h), (k), (n) TDOS and (c), (f), (i), (l), (o) PDOS of $Mo_2C_{1-x}N_x$ ($x = 0$, 0.25, 0.5, 0.75, 1). (p) BZ and its projections on (001), (010), and (100) surfaces.

concentrations of 0, 0.25, 0.5, 0.75, and 1, as presented in Fig. 2. Figures 2(a), 2(d), 2(g), 2(j), and 2(m) show the electronic band structures along high-symmetry paths [defined in Fig. 2(p)] for each doping level. In all cases, multiple bands cross the Fermi level, confirming the metallic nature of $Mo_2C_{1-x}N_x$ across the entire doping range. Although the overall band structure shapes of $Mo_2C_{1-x}N_x$ are similar throughout the entire N-doping range, the Fermi level shifts upwards as the N concentration increases. Because the band near Fermi level is dense and multiple bands cross, we further provide a direct comparison of the same representative band (the lowest valence band) for different N-doping levels (Fig. S4 of the SM [33]), which makes the doping-induced upward shift of Fermi level more transparent. This is naturally expected because each N substitution introduces one additional valence electron compared with C, thereby filling states near the Fermi level. Figures 2(b), 2(e), 2(h), 2(k), and 2(n) present the total density of states (TDOS) together with its element-resolved components for each doping level. The data reveal that TDOS around the Fermi level are overwhelmingly contributed by Mo atoms; quantitative analysis shows Mo accounts for more than 94% of the TDOS at the Fermi level. A notable feature emerges at a N-doping concentration of $x = 0.75$, where the Fermi level shifts upwards and approaches a van Hove singularity (vHs) peak. Consequently, the TDOS of $Mo_2C_{0.25}N_{0.75}$ is significantly enhanced, increasing from 6.24 states/eV for α-Mo_2C to approximately 10.28 states/eV. This enhancement in the TDOS is expected to strengthen EPC and is beneficial for superconducting properties in the N-doped system. The partial DOS (PDOS), shown in Figs. 2(c), 2(f), 2(i), 2(l), and 2(o), reveal that the

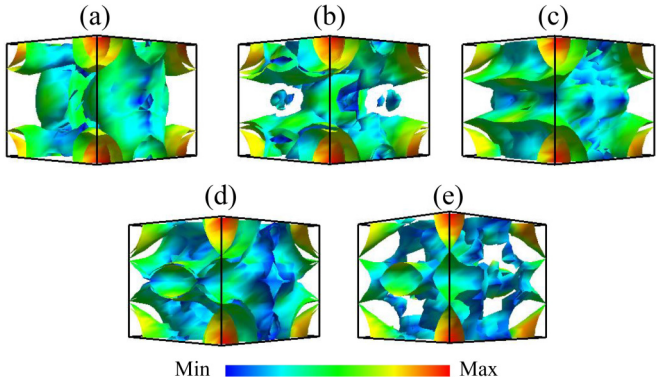

FIG. 3. (a)–(e) The Fermi surfaces of $Mo_2C_{1-x}N_x$ ($x = 0$, 0.25, 0.5, 0.75, 1) weighted by the Fermi velocity v_F.

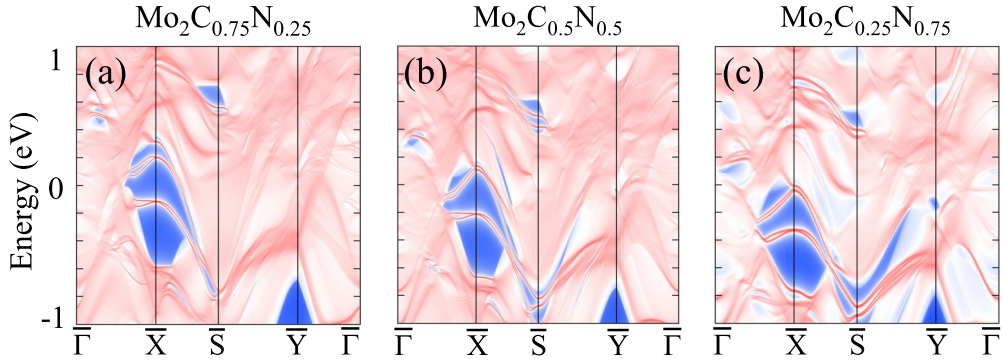

FIG. 4. (a)–(c) TSSs of $Mo_2C_{1-x}N_x$ ($x = 0.25, 0.5, 0.75$) on the (001) surface.

five Mo-4*d* orbitals contribute nearly equally to the states near the Fermi level across all doping levels. This suggests a relatively weak crystal field effect in $Mo_2C_{1-x}N_x$, regardless of N concentration. Collectively, these results confirm that the Mo-4*d* electrons dominate the electronic states near the Fermi level, playing a crucial role in the superconducting behavior of N-doped α-Mo_2C. Figures 3(a)–3(e) show the Fermi surfaces (FSs) weighted by the Fermi velocity (v_F) for $Mo_2C_{1-x}N_x$ ($x = 0, 0.25, 0.5, 0.75, 1$), where the magnitude of the v_F is encoded by the color scale, with the redder regions corresponding to larger v_F, steeper band slopes, stronger electronic dispersion, faster carrier motion, and higher conductivity. More importantly, increasing the N concentration induces a clear reconstruction of the FS, which manifests in the appearance or disappearance of the Fermi pockets (see also Fig. S5 of the SM [33]), indicating a change in FS topology. Such a topology change of the FS, driven by a band edge crossing the Fermi level, is characteristic of a Lifshitz transition. This FS reconstruction provides an essential electronic structure basis for understanding the doping dependent evolution of the superconducting properties discussed below.

Molybdenum atoms are known to exhibit strong spin-orbit coupling (SOC), which can give rise to topologically nontrivial electronic states. To examine this possibility in $Mo_2C_{1-x}N_x$ ($x = 0, 0.25, 0.5, 0.75, 1$), we compare the electronic band structures calculated without and with SOC, as shown in Figs. S6(a–j) of the SM [33]. With SOC, the previously degenerate crossings between the highest occupied band (blue) and the lowest unoccupied band (red) are lifted, producing finite direct gap openings along high-symmetry paths. Representative localized energy gap cracking is clearly shown in Fig. S6 of the SM [33]. Importantly, to assess whether such a separation persists beyond high-symmetry lines, we further evaluate the gap magnitude throughout the irreducible Brillouin zone and summarize the resulting distribution in Fig. S7 of the SM [33]. The finite gap distribution indicates that SOC induces a global separation gap between the highest occupied and lowest unoccupied bands across the irreducible Brillouin zone, which provides the band-gap prerequisite for defining the topological invariant Z_2 discussed below. To further verify the topological properties of $Mo_2C_{1-x}N_x$ ($x = 0, 0.25, 0.5, 0.75, 1$), we construct the Maximally Localized Wannier Functions (MLWFs) by using Wannier90 to obtain accurate tight-binding Hamiltonians. *d* orbitals of Mo atoms and *p* orbitals of C/N atoms are chosen as the initial projections. The Wannier-interpolated band structures show excellent agreement with the first principles results as shown in Fig. S8 of the SM [33], ensuring the reliability of the derived tight-binding models. And the Wilson loop method [38] is employed to calculate the topological invariants of the occupied bands below the energy gap opened between the highest valence and lowest conduction states, as shown in Fig. S6 of the SM [33]. For three dimensional systems, the topological classification is characterized by the strong index (ν_0) and three weak indices ($\nu_1\nu_2\nu_3$) [39,40]. The results reveal a distinct doping induced topological oscillation: $Mo_2C_{1-x}N_x$ at ($x = 0$) is topologically trivial materials with (0;000), while the nitrogen is introduced leading to topologically nontrivial materials (1;000) for $x = 0.25$, 0.5, and 0.75. Upon further doping to full substitution ($x = 1$), the system reverts to topologically trivial materials (0;000). These results provide a compelling platform for exploring doping controlled topological materials. A defining feature of the topologically nontrivial materials is the existence of topological surface states (TSS). Based on the MLWFs, the surface spectral functions of a semi-infinite system is calculated using the iterative Green's function method. Figures 4(a)–4(c) present the TSSs on the (001) surface of $Mo_2C_{1-x}N_x$ ($x = 0.25, 0.5, 0.75$) along high-symmetry paths in the projected 2D Brillouin zone of Fig. 2(p), where a Rashba-like TSS is clearly resolved at the $\bar{X}$ point within the bulk energy gap. The corresponding TSSs on the (010) and (100) surfaces are provided in Fig. S9 of the SM [33]. These Rashba-like TSSs should be directly observable via angle-resolved photoemission spectroscopy (ARPES) [41].

C. Electron-phonon coupling and superconductivity

To investigate the vibrational properties of N-doped α-Mo_2C, we analyze both the phonon dispersion [Figs. 5(a), 5(d), 5(g), 5(j), and 5(m)] and the phonon DOS (PhDOS) [Figs. 5(b), 5(e), 5(h), 5(k), and 5(n)] for $Mo_2C_{1-x}N_x$ ($x = 0$, 0.25, 0.5, 0.75, 1). The phonon spectra exhibit no imaginary frequencies throughout the entire frequency range, which indicates that varying the N concentration does not compromise the dynamic stability of the $Mo_2C_{1-x}N_x$. To better characterize the vibrational behavior, the phonon spectra are divided into two frequency regions, including $0-310\,cm^{-1}$ and $311-700\,cm^{-1}$. In the lower range ($0-310\,cm^{-1}$), Mo atom vibrations are dominant. The higher range ($311-700\,cm^{-1}$)

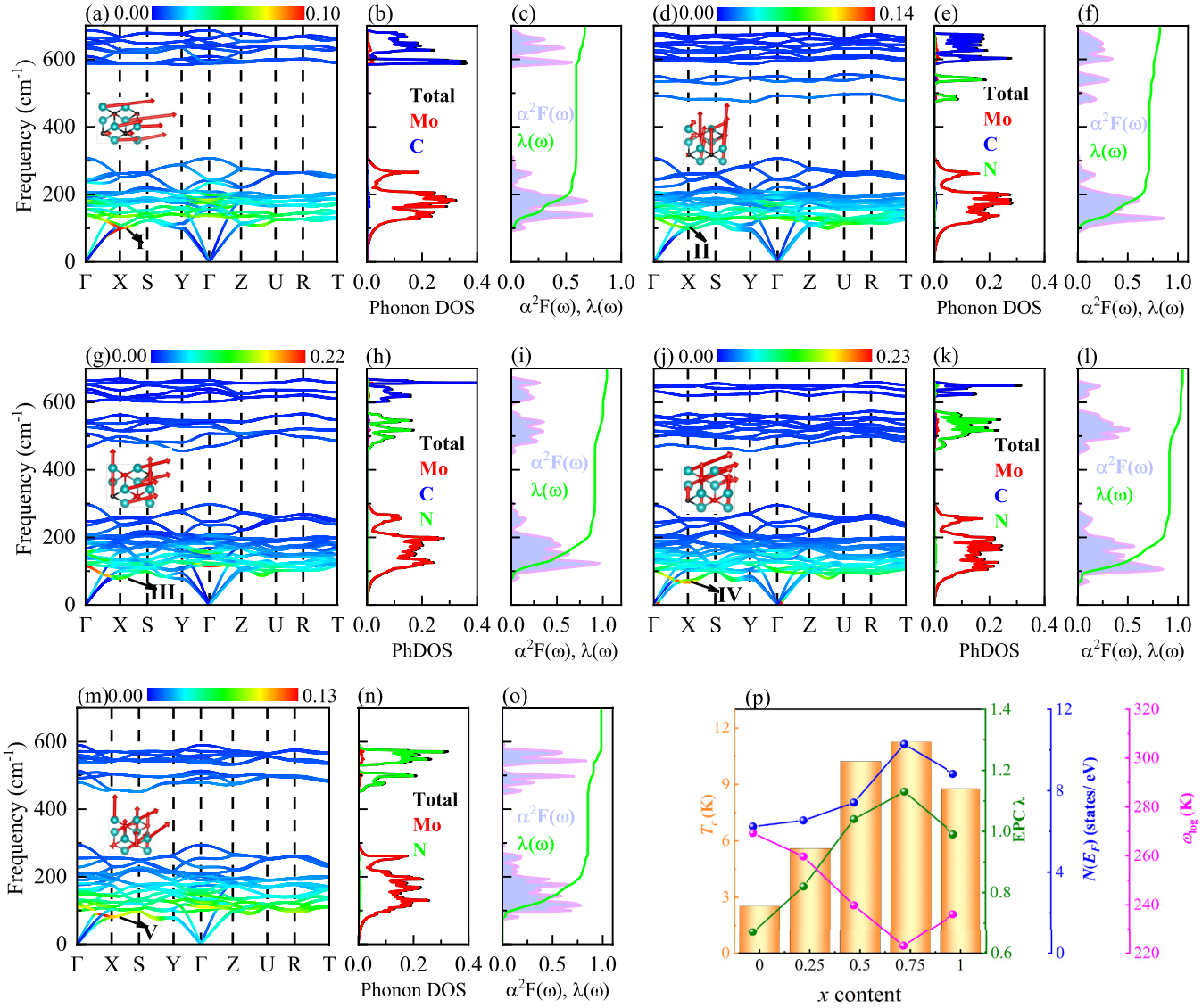

FIG. 5. (a), (d), (g), (j), and (m) Phonon dispersion weighted by the magnitude of EPC $\lambda_{\mathbf{q}\nu}$ for $Mo_2C_{1-x}N_x$ ($x = 0, 0.25, 0.5, 0.75, 1$) where the coupling strength gradually increases as the color changes from blue to red. (b), (e), (h), (k), and (n) Total PhDOS of $Mo_2C_{1-x}N_x$ ($x = 0, 0.25, 0.5, 0.75, 1$) and the total PhDOS of each element. (c), (f), (i), (l), and (o) Eliashberg spectral function $\alpha^2F(\omega)$ and cumulative frequency-dependent EPC function $\lambda(\omega)$ of $Mo_2C_{1-x}N_x$ ($x = 0, 0.25, 0.5, 0.75, 1$). (p) Variation of T_c, λ, $\omega_{\log}$, and $N(E_F)$ with the increase of N-doping concentration.

mainly involves vibrations from C and N atoms. An increase in N concentration leads to a noticeable softening of certain optical phonon branches in the high-frequency region, which arise mainly from the vibrations of N atoms because of the larger atomic mass of N compared to C. Consequently, these modes are energetically separated and shifted to lower frequencies. This characteristic may affect the superconductivity of $Mo_2C_{1-x}N_x$ ($x = 0, 0.25, 0.5, 0.75, 1$).

The phonon dispersion weighted by the magnitude of EPC $\lambda_{\mathbf{q}\nu}$ [Figs. 5(a), 5(d), 5(g), 5(j), and 5(m)], along with the Eliashberg spectral function $\alpha^2F(\omega)$ and its cumulative frequency dependent EPC function $\lambda(\omega)$ [Figs. 5(c), 5(f), 5(i), 5(l), and 5(o)], clearly demonstrate that the low-frequency phonon modes dominate the EPC in $Mo_2C_{1-x}N_x$ ($x = 0$, 0.25, 0.5, 0.75, 1). These modes contribute more than 86% of the total EPC strength, whereas contributions from high-frequency phonons are negligible. Therefore, the influence of N-doping induced high-frequency optical phonon branching softening on the superconducting properties of Mo_2C system can be ignored. By analyzing low-frequency phonon spectra of $Mo_2C_{1-x}N_x$ ($x = 0, 0.25, 0.5, 0.75, 1$), it is found that the EPC is relatively strong below the frequency of 200 cm^{-1} as shown in Figs. 5(a), 5(d), 5(g), 5(j), and 5(m). The progressive softening of phonon modes in the low-frequency region ($0 - 200\,cm^{-1}$) with increasing N concentration, as shown in the circled in green (Fig. S10 of the SM [33]), contributes to enhance the EPC and thereby raises T_c [42–45]. Additionally, by calculating the vibration mode at the high-symmetry point X for $Mo_2C_{1-x}N_x$ ($x = 0, 0.25, 0.5, 0.75, 1$) [I, II, III, IV, and V in Figs. 5(a), 5(d), 5(g), 5(j), and 5(m)], which

TABLE II. The total EPC constant λ, the logarithmically averaged phonon frequency $\omega_{\log}$ (K), and T_c (K) for $Mo_2C_{1-x}N_x$ ($x = 0$, 0.25, 0.5, 0.75, 1).

Materials	λ	$\omega_{\log}$	T_c
α-Mo_2C	0.67	269.33	2.53
$Mo_2C_{0.75}N_{0.25}$	0.82	259.75	5.61
$Mo_2C_{0.5}N_{0.5}$	1.04	239.80	10.22
$Mo_2C_{0.25}N_{0.75}$	1.16	222.46	11.78
Mo_2N	0.99	236.13	8.78

exhibits strong coupling and simultaneous phonon softening, it is evident that Mo atoms vibrate more strongly relative to C/N atoms [as shown in the inset of the Figs. 5(a), 5(d), 5(g), 5(j), and 5(m)]. This observation indicates that the vibrations of Mo atoms indeed play a major role in the EPC. Combined with the electronic structure analysis, these findings confirm that the dominant contribution to EPC originates from the coupling between the low-frequency vibrational modes of Mo atoms and the Mo-4*d* electrons. This coupling mechanism is key to understanding the doping-dependent superconducting behavior of N-doped α-Mo_2C.

Based on $\alpha^2F(\omega)$, we quantitatively determine the logarithmically averaged phonon frequency ($\omega_{\log}$) and the total EPC constant (λ) for $Mo_2C_{1-x}N_x$ ($x = 0$, 0.25, 0.5, 0.75, 1), as shown in Table II. According to $\mu^* \approx 0.26N(E_F)/[1 + N(E_F)]$, where $N(E_F)$ is the electronic DOS at the Fermi level [46–48], μ^* is 0.2 when rounded to one decimal place. The T_c is calculated using the Allen–Dynes modified McMillan equation, yielding an increase in T_c from 2.53 ($x = 0$) to a maximum of 11.78 ($x = 0.75$), then slightly decreasing to 8.78 ($x = 1$) and showing a dome-shaped dependence of T_c on N-doping, which is in excellent agreement with experimental results [22]. To more clearly expose the microscopic origin of the superconducting dome and its connection to the doping-induced electronic reconstruction discussed in Sec. III B, Fig. 5(p) summarizes the calculated T_c, λ, $\omega_{\log}$ and $N(E_F)$ as functions of the N concentration. Within the Allen-Dynes framework, the evolution of T_c is governed by the competition between the EPC strength λ, the logarithmically averaged frequency $\omega_{\log}$, and the electronic DOS at the Fermi level $N(E_F)$. As shown in Fig. 5(p), for $x \leqslant 0.75$, $N(E_F)$ increases monotonically with doping, which is consistent with the FS reconstruction/Lifshitz physics. And the Mo-dominated low-frequency phonon branches that provide the dominant contribution to the total EPC, exhibit a clear softening (highlighted by the green-circled regions in Fig. S10 of the SM [33]). Therefore, the enhancement of λ driven jointly by the increased $N(E_F)$ and the softening of the relevant low-energy modes outweighs the reduction in $\omega_{\log}$, leading to a monotonic increase of T_c. Upon further increasing the doping to $x = 1$, the trend becomes nonmonotonic. The $N(E_F)$ decreases compared with that at $x = 0.75$ Fig. 5(p), while the Mo-dominated low-frequency modes partially harden, which reduces the mode resolved EPC contributions. Consequently, the total EPC constant decreases from $\lambda = 1.16$ at $x = 0.75$ to $\lambda = 0.99$ at $x = 1$, and together with the concomitant increase in $\omega_{\log}$ this results in a suppressed T_c in fully substituted Mo_2N. To ensure the reliability of these conclusions, we carried out systematic numerical validations, including additional DOS calculations at finer doping intervals (Fig. S11 of the SM [33]), k/q-mesh convergence tests for EPC calculations to confirm that the λ values is not an artifact of coarse sampling (Fig. S12 of the SM [33]), and μ^* sensitivity analysis showing that the dome-shaped $T_c(x)$ trend persists for the values $\mu^* = 0.10$, 0.13 and 0.20 (Fig. S13 of the SM [33]). Taken together, these checks establish that the reported $T_c(x)$ dome and its microscopic interpretation are robust with respect to both numerical convergence and reasonable choices of model parameters.

IV. CONCLUSION

In conclusion, we have carried out a comprehensive first-principles investigation of the electronic structure, topological properties, and the microscopic origin of the enhanced superconductivity in N-doped orthorhombic α-Mo_2C. The orthorhombic framework remains stable across the entire doping range, while N substitution electron dopes the system and shifts the Fermi level upward, leading to a pronounced FS reconstruction accompanied by a Lifshitz transition and a trivial-nontrivial-trivial topological evolution, as confirmed by Wannier-based Z_2 invariants. Consistent with bulk-boundary correspondence, the calculated (001) surface spectra for $x = 0.25$, 0.50, and 0.75 reveal Rashba-like TSSs at $\bar{X}$ point, which should be directly testable by ARPES. The dome-shaped $T_c(x)$ is quantitatively explained by our mode-resolved EPC analysis. For $x \leqslant 0.75$, the increase of $N(E_F)$ together with the softening of Mo-dominated low-frequency phonons enhances λ and raises T_c, whereas for ($x > 0.75$), the reduction of $N(E_F)$ and partial hardening of these modes suppress λ and T_c. The dominant EPC originates from Mo-*d* electrons coupling to low-energy Mo vibrations, and μSR measurements could further probe the superconducting state across doping.

ACKNOWLEDGMENTS

We thank helpful discussions with Na Jiao and Jie Zhang. This work is supported by the National Natural Science Foundation of China (Grants No. 12074213 and No. 11574108), National Key R&D Program of China (Grant No. 2022YFA1403103), the Major Basic Program of Natural Science Foundation of Shandong Province (Grant No. ZR2021ZD01), the Natural Science Foundation of Shandong Province (Grant No. ZR2023MA082), and the Project of Introduction and Cultivation for Young Innovative Talents in Colleges and Universities of Shandong Province.

DATA AVAILABILITY

The data that support the findings of this article are not publicly available. The data are available from the authors upon reasonable request.

[1] R. H. Willens, E. Buehler, and B. T. Matthias, Superconductivity of the transition-metal carbides, Phys. Rev. **159**, 327 (1967).

[2] N. Morton, B. James, G. Wostenholm, D. Pomfret, M. Davies, and J. Dykins, Superconductivity of molybdenum and tungsten carbides, J. Less-Common Met. **25**, 97 (1971).

[3] J. Häglund, A. Fernández Guillermet, G. Grimvall, and M. Körling, Theory of bonding in transition-metal carbides and nitrides, Phys. Rev. B **48**, 11685 (1993).

[4] S. A. Rasaki, B. Zhang, K. Anbalgam, T. Thomas, and M. Yang, Synthesis and application of nano-structured metal nitrides and carbides: A review, Prog. Solid State Chem. **50**, 1 (2018).

[5] K. N. Dinh, Q. Liang, C.-F. Du, J. Zhao, A. I. Y. Tok, H. Mao, and Q. Yan, Nanostructured metallic transition metal carbides, nitrides, phosphides, and borides for energy storage and conversion, Nano Today **25**, 99 (2019).

[6] S. Posada-Pérez, F. Viñes, P. J. Ramirez, A. B. Vidal, J. A. Rodriguez, and F. Illas, The bending machine: CO_2 activation and hydrogenation on δ-MoC(001) and β-Mo_2C(001) surfaces, Phys. Chem. Chem. Phys. **16**, 14912 (2014).

[7] Y. Ma, G. Guan, X. Hao, J. Cao, and A. Abudula, Molybdenum carbide as alternative catalyst for hydrogen production – A review, Renew. Sustain. Energy Rev. **75**, 1101 (2017).

[8] C. Wan, Y. N. Regmi, and B. M. Leonard, Multiple phases of molybdenum carbide as electrocatalysts for the hydrogen evolution reaction, Angew. Chem., Int. Ed. **53**, 6407 (2014).

[9] G. García, M. Roca-Ayats, O. Guillén-Villafuerte, J. Rodríguez, M. Arévalo, and E. Pastor, Electrochemical performance of α-Mo_2C as catalyst for the hydrogen evolution reaction, J. Electroanal. Chem. **793**, 235 (2017).

[10] X. Huang, J. Wang, H. Bing Tao, H. Tian, Z. Zhang, and H. Xu, Unraveling the oxide layer on Mo_2C as the active center for hydrogen evolution reaction, J. Catal. **389**, 461 (2020).

[11] L. Jin, Z. Pan, L. Wang, and X. Ji, Effect of thermal annealing on phase structure and hydrogen evolution reaction of molybdenum carbide thin films prepared by co-sputtering, Thin Solid Films **809**, 140579 (2025).

[12] M. Nagai and K. Matsuda, Low-temperature water–gas shift reaction over cobalt–molybdenum carbide catalyst, J. Catal. **238**, 489 (2006).

[13] J. A. Schaidle, A. C. Lausche, and L. T. Thompson, Effects of sulfur on Mo_2C and Pt/Mo_2C catalysts: Water gas shift reaction, J. Catal. **272**, 235 (2010).

[14] E. Parthé and V. Sadogopan, The structure of dimolybdenum carbide by neutron diffraction technique, Acta Crystallogr. **16**, 202 (1963).

[15] Y. Ge, H. Song, K. Bao, S. Ma, L. Li, Q. Tao, P. Zhu, B. Liu, D. Duan, and T. Cui, A novel hard superconductor obtained in dimolybdenum carbide (Mo_2C) with Mo–C octahedral structure, J. Alloys Compd. **881**, 160631 (2021).

[16] J. Bardeen, L. N. Cooper, and J. R. Schrieffer, Theory of superconductivity, Phys. Rev. **108**, 1175 (1957).

[17] R. Jiang, J. Fan, L. Hu, Y. Dou, X. Mao, and D. Wang, Electrochemically synthesized N-doped molybdenum carbide nanoparticles for efficient catalysis of hydrogen evolution reaction, Electrochim. Acta **261**, 578 (2018).

[18] J. Chen, H. Yang, X. Xu, Z. Su, Y. Guo, and Q. Wang, Mo_2C-based electrocatalyst with filter paper derived N-doped mesoporous carbon as matrix for H_2 production, Appl. Surf. Sci. **455**, 187 (2018).

[19] M. Yang, D. Guo, T. Zhang, G. Liu, N. Wu, A. Qin, X. Liu, and H. Mi, Controlled synthesis of ultrafine β-Mo_2C nanoparticles encapsulated in N-doped porous carbon for boosting lithium storage kinetics, ACS Omega **6**, 29609 (2021).

[20] H. Min, X. Zhang, H. Shu, L. Luo, X. Zeng, Y. Liao, Z. Chen, and X. Wang, Mo_2C quantum dots inlaid in nitrogen-doped carbon nanofibers as free-standing anodes with long-term stability K-ion storage, J. Alloys Compd. **888**, 161498 (2021).

[21] Z. Zhang, Y. Fang, D. Wang, S. Zhang, G. Mu, and F. Huang, One-step synthesis of nitrogen-rich $Mo_2C_{1-x}N_x$ solid solution with enhanced superconductivity, J. Mater. Chem. C **8**, 2682 (2020).

[22] L. Li, L. Shi, L. Zeng, K. Li, P. Yu, K. Wang, C. Zhang, R. Chen, Z. Xiang, Y. Zhang, and H. Luo, A simple urea approach to N-doped α-Mo_2C with enhanced superconductivity, Chin. Phys. Lett. **41**, 107401 (2024).

[23] N.-N. Zhao, P.-J. Guo, X.-Q. Lu, Q. Han, K. Liu, and Z.-Y. Lu, Topological properties of Mo_2C and W_2C superconductors, Phys. Rev. B **101**, 195144 (2020).

[24] G. Kresse and J. Furthmüller, Efficient iterative schemes for *ab initio* total-energy calculations using a plane-wave basis set, Phys. Rev. B **54**, 11169 (1996).

[25] P. Giannozzi, S. Baroni, N. Bonini, M. Calandra, R. Car, C. Cavazzoni, D. Ceresoli, G. L. Chiarotti, M. Cococcioni, I. Dabo, A. Dal Corso, S. de Gironcoli, S. Fabris, G. Fratesi, R. Gebauer, U. Gerstmann, C. Gougoussis, A. Kokalj, M. Lazzeri, L. Martin-Samos, *et al.*, QUANTUM ESPRESSO: A modular and open-source software project for quantum simulations of materials, J. Phys.: Condens. Matter **21**, 395502 (2009).

[26] G. Kresse and D. Joubert, From ultrasoft pseudopotentials to the projector augmented-wave method, Phys. Rev. B **59**, 1758 (1999).

[27] J. P. Perdew, K. Burke, and M. Ernzerhof, Generalized gradient approximation made simple, Phys. Rev. Lett. **77**, 3865 (1996).

[28] Q. Wu, S. Zhang, H.-F. Song, M. Troyer, and A. A. Soluyanov, WannierTools: An open-source software package for novel topological materials, Comput. Phys. Commun. **224**, 405 (2018).

[29] M. P. L. Sancho, J. M. L. Sancho, J. M. L. Sancho, and J. Rubio, Highly convergent schemes for the calculation of bulk and surface Green functions, J. Phys. F: Met. Phys. **15**, 851 (1985).

[30] N. Marzari, A. A. Mostofi, J. R. Yates, I. Souza, and D. Vanderbilt, Maximally localized Wannier functions: Theory and applications, Rev. Mod. Phys. **84**, 1419 (2012).

[31] I. Souza, N. Marzari, and D. Vanderbilt, Maximally localized Wannier functions for entangled energy bands, Phys. Rev. B **65**, 035109 (2001).

[32] C. Franchini, R. Kováčik, M. Marsman, S. Sathyanarayana Murthy, J. He, C. Ederer, and G. Kresse, Maximally localized Wannier functions in $LaMnO_3$ within PBE + U, hybrid functionals and partially self-consistent GW: An efficient route to construct *ab initio* tight-binding parameters for e_g perovskites, J. Phys.: Condens. Matter **24**, 235602 (2012).

[33] See Supplemental Material at http://link.aps.org/supplemental/10.1103/fssg-1b79 for calculation details, structures and properties of two different configurations of $Mo_2C_{0.5}N_{0.5}$, the lowest valence band, FSs, band structures without/with SOC, global

gap, band structures by DFT and MLWF for $Mo_2C_{1-x}N_x$ (x = 0, 0.25, 0.5, 0.75, 1), TSSs of $Mo_2C_{1-x}N_x$ (x = 0.25, 0.5, 0.75) on (010) and (100) surfaces, comparison of phonon spectra, DOS at the Fermi level of $Mo_2C_{1-x}N_x$ (x = 0, 0.125, 0.25, 0.375, 0.5, 0.625, 0.75, 0.825, 1), λ as a function of degauss for different k-meshes and q-meshes for Mo_2C and T_c as a function of N content (x) for different Coulomb pseudopotentials, which included Refs. [34–36].

[34] W. L. McMillan, Transition temperature of strong-coupled superconductors, Phys. Rev. **167**, 331 (1968).

[35] R. C. Dynes, McMillan's equation and the T_c of superconductors, Solid State Commun. **10**, 615 (1972).

[36] P. B. Allen and R. C. Dynes, Transition temperature of strong-coupled superconductors reanalyzed, Phys. Rev. B **12**, 905 (1975).

[37] T. Epicier, J. Dubois, C. Esnouf, G. Fantozzi, and P. Convert, Neutron powder diffraction studies of transition metal hemicarbides M_2C_{1-x}—II. *In situ* high-temperature study on W_2C_{1-x} and Mo_2C_{1-x}, Acta Metall. **36**, 1903 (1988).

[38] R. Yu, X. L. Qi, A. Bernevig, Z. Fang, and X. Dai, Equivalent expression of $\mathbb{z}_2$ topological invariant for band insulators using the non-Abelian Berry connection, Phys. Rev. B **84**, 075119 (2011).

[39] L. Fu, C. L. Kane, and E. J. Mele, Topological insulators in three dimensions, Phys. Rev. Lett. **98**, 106803 (2007).

[40] L. Fu and C. L. Kane, Topological insulators with inversion symmetry, Phys. Rev. B **76**, 045302 (2007).

[41] B. Lv, T. Qian, and H. Ding, Angle-resolved photoemission spectroscopy and its application to topological materials, Nat. Rev. Phys. **1**, 609 (2019).

[42] C. Si, Z. Liu, W. Duan, and F. Liu, First-principles calculations on the effect of doping and biaxial tensile strain on electron-phonon coupling in graphene, Phys. Rev. Lett. **111**, 196802 (2013).

[43] P.-F. Liu, J. Li, X.-H. Tu, H. Yin, B. Sa, J. Zhang, D. J. Singh, and B.-T. Wang, Prediction of superconductivity and topological aspects in single-layer $\beta - Bi_2Pd$, Phys. Rev. B **102**, 155406 (2020).

[44] X.-H. Tu, T. Bo, P.-F. Liu, W. Yin, N. Hao, and B.-T. Wang, Superconductivity in Mo–P compounds under pressure and in double-Weyl semimetal Hex-MoP_2, Phys. Chem. Chem. Phys. **24**, 7893 (2022).

[45] Y.-L. Han, H.-D. Liu, N. Jiao, M.-M. Zheng, H.-Y. Lu, B.-T. Wang, and P. Zhang, Theoretical prediction of superconductivity in two-dimensional hydrogenated metal diboride: M_2B_2H (M = Al, Mg, Mo, W), Phys. Rev. Mater. **7**, 114802 (2023).

[46] K. H. Bennemann and J. W. Garland, Theory for superconductivity in d-band metals, AIP Conf. Proc. **4**, 103 (1972).

[47] F. Zheng, X.-B. Li, P. Tan, Y. Lin, L. Xiong, X. Chen, and J. Feng, Emergent superconductivity in two-dimensional $NiTe_2$ crystals, Phys. Rev. B **101**, 100505(R) (2020).

[48] D. Wu, Y. Lin, L. Xiong, J. Li, T. Luo, D. Chen, and F. Zheng, Enhanced superconductivity in bilayer $PtTe_2$ by alkali-metal intercalations, Phys. Rev. B **103**, 224502 (2021).